TU Delft

Delft University of Technology

Design and testing of a multi-electrode apodized acousto-optic filter for arbitrary polarized light

Dupont, Samuel; Kastelik, Jean Claude; Vanhamel, Jurgen

DOI
10.1364/AO.514229

Publication date
2024

Document Version
Final published version

Published in
Applied Optics

Citation (APA)
Dupont, S., Kastelik, J. C., & Vanhamel, J. (2024). Design and testing of a multi-electrode apodized acousto-optic filter for arbitrary polarized light. *Applied Optics*, *63*(10), 2487-2493. https://doi.org/10.1364/AO.514229

Important note
To cite this publication, please use the final published version (if applicable).
Please check the document version above.

Copyright
Other than for strictly personal use, it is not permitted to download, forward or distribute the text or part of it, without the consent of the author(s) and/or copyright holder(s), unless the work is under an open content license such as Creative Commons.

Takedown policy
Please contact us and provide details if you believe this document breaches copyrights.
We will remove access to the work immediately and investigate your claim.

This work is downloaded from Delft University of Technology.
For technical reasons the number of authors shown on this cover page is limited to a maximum of 10.

Green Open Access added to TU Delft Institutional Repository

'You share, we take care!' - Taverne project

https://www.openaccess.nl/en/you-share-we-take-care

Otherwise as indicated in the copyright section: the publisher is the copyright holder of this work and the author uses the Dutch legislation to make this work public.

applied optics

Design and testing of a multi-electrode apodized acousto-optic filter for arbitrary polarized light

Samuel Dupont,[1,2,*] Jean-Claude Kastelik,[1,2] and Jurgen VanHamel[3,4]

[1]Université Polytechnique Hauts-de-France, CNRS, University of Lille, ISEN, Centrale Lille, UMR 8520, Institut d'Électronique de Microélectronique et de Nanotechnologie (IEMN), F-59313 Valenciennes, France
[2]INSA Hauts de France, F-59313 Valenciennes, France
[3]TU Delft Faculty of Aerospace Engineering, Section Space Systems Engineering, 2629 HS Delft, Netherlands
[4]KU Leuven, Electronic Circuits and Systems, Geel 2440, Belgium
*Samuel.dupont@uphf.fr

Received 24 November 2023; revised 9 February 2024; accepted 3 March 2024; posted 5 March 2024; published 21 March 2024

We present an original acousto-optic tunable filter that is able to filter visible light from 400 to 650 nm and is designed to interact simultaneously with two polarizations. The filter shows an adjustable optical bandwidth and apodization capabilities. These features make it suitable for practical spectroscopic applications. Experimental validation is also presented. © 2024 Optica Publishing Group

https://doi.org/10.1364/AO.514229

1. INTRODUCTION

The acousto-optic effect that appears in some optical materials can be employed to design versatile devices. In elasto-optical materials, it is possible to obtain a periodic modulation of the refractive index under the effect of an ultrasonic wave [1]; this modulation acts as a diffraction grating for the incident light. Acousto-optical components have been developed on the basis of this principle [2]: numerous developments have enabled the conception of modulators, deflectors, frequency shifters, and filters [3]. During the acousto-optical interaction, the wavelength of the diffracted light can be adjusted by tuning the frequency of the acoustic wave. This tunability is a key feature of acousto-optical tunable filters (AOTFs [4]) and allows fast and accurate control of the transmitted wavelength. AOTFs are devices that help control light transmission. A non-collinear AOTF, as the name suggests, is an AOTF for which the incident light and the directions of propagation of the acoustic waves are not parallel [5]. This configuration allows for greater flexibility and tunability in the handling of transmitted light. Non-collinear AOTFs find applications in various fields such as spectroscopy, telecommunications, and imaging. They are especially useful in situations where a quick wavelength adjustment is required.

AOTFs are traditionally designed according to the principle of the parallel tangent anisotropic interaction (also referred to as noncritical phase matching, NPM). This configuration has a narrow filtering bandwidth, together with a high operating bandwidth [6,7]. However, the anisotropic acousto-optical interaction requires the use of a linearly polarized incident beam whose polarization axis is either collinear or orthogonal to the acousto-optical interaction plane. This renders them less effective for applications with a non-polarized optical incident beam.

Moreover, the theoretical study of the optical bandwidth of a filter indicates an inversely proportional relationship with the length of the transducer. An acousto-optic component has a cardinal sinus-like response that composes a main lobe and secondary lobes [8]. This specificity is a sign of the finite dimension of the transducer generating the acoustic waves. The secondary lobes may result in optical crosstalk that is undesirable when analyzing two optical tones close to each other.

From a practical point-of-view, there are many applications where optical filtering is performed on partially polarized light. Assessing the degree of polarization of light is a useful aspect of scattering properties of aerosols [9]. Additionally, multiple optical wavelength filtering is necessary to meet the requirements of a spectral analysis of atmospheric gases to distinguish gases such as NO_2 [10].

For effectiveness in such a context, the design of an AOTF requires two particular characteristics: (1) it needs to be able to filter arbitrary polarized light and (2) it must allow for adjusting the optical bandwidth or filtering out of multiple optical wavelengths. Unfortunately, these two aspects are not possible with the traditional NPM configuration.

On one hand, the capacity to interact with incident beams of any polarization is possible for a particular design of the interaction: the dual (or simultaneous) interaction. In this configuration, depending on whether the incident beam is coupled to the ordinary or the extraordinary mode, the diffracted beam will be either "downshifted" (order −1) or "upshifted" (order +1). The case of an incident beam with different states of polarization will result in two diffracted beams in both orders (+1 and −1), with a relative proportion which reflects the incident

polarization content of the incident beam [11]. On the other hand, the bandwidth control or multiple wavelength operation capability is made possible with the usage of a multi-electrode piezoelectric transducer [12]. We evaluate the possibility to combine these two features.

In this paper, we describe the design of an original multi-electrode component that is able to simultaneously diffract two incident beams of orthogonal polarizations and present an apodized filter response. The originality of these combined features makes it effective for spectroscopic study of gases or scattering aerosols. We present the characteristics of the dual interaction, as well as the advantages related to the multi-electrode configuration. Then a description of the different stages of the design of the original component is proposed. Finally, the experimental results are presented: we focus on the original experimental results that establish the apodization capabilities of the proposed design.

2. ANISOTROPIC ACOUSTO-OPTIC DIFFRACTION IN PARATELLURITE

To start with, we briefly recall the well-known acousto-optic interaction mechanism in paratellurite: the acousto-optical interaction referred to as "anisotropic" concerns the diffraction of an optical wave by an acoustic wave with a change of polarization [13]. This interaction is implemented in birefringent crystals. Paratellurite (TeO_2) is a case of birefringent crystal: it is a positive uniaxial crystal. TeO_2 usage is widespread in acousto-optics due to its transparency from near UV to medium infrared and its high diffraction efficiency. The anisotropic interaction can definitely present very high diffraction efficiencies in this crystal under the Bragg synchronism condition (close to 100% in practice), provided that the incident optical beam is fully coupled to one of the two optical modes of the crystal: the so-called ordinary or extraordinary mode. This implies that the incident optical beam is polarized linearly and oriented collinearly or orthogonally to the plane of the acousto-optical interaction. The acoustic diffraction grating is generated by a radiofrequency (RF) signal applied to a piezoelectric transducer bonded to the crystal. The synchronism of the interaction is obtained when the momentum matching condition is obtained; that is,

$$\mathbf{k}_d = \mathbf{k}_i \pm \mathbf{K},$$

with $|\mathbf{K}| = 2\pi f/V$ being the acoustic wave vector and $|\mathbf{k}_{d(/i)}| = 2\pi n_{d(/i)}/\lambda_0$ being the diffracted (/incident) optical wave vectors; f is the RF signal frequency, V is the acoustic wave velocity, $n_{d(/i)}$ is the refractive index of the diffracted (/incident) light, and λ_0 is the optical wavelength in vacuum.

Figure 1 illustrates the case of filtering two arbitrary polarized optical signals of the frequency υ_O and υ_1. A particular optical wavelength corresponds to a particular acoustic frequency at synchronism. As illustrated in this figure, the grating generated by the acoustic frequency f_O diffracts the incident optical beam of the wavelength υ_O and with no particular polarization simultaneously in two opposite directions. For example, for an incident optical beam of linear polarization oriented at 45° to the interaction plane, the same diffraction efficiency is expected in the +1 and −1 diffraction orders. In other words, such a device allows the spectral and polarimetric composition of any

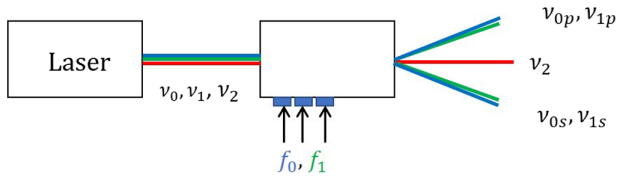

Fig. 1. Polarization insensitive multiple wavelength acousto-optical filtering principle illustration.

source to be studied and quantified by decomposing it into two orthogonally polarized and angularly separated optical beams.

Figure 2 shows the wave vector diagram of the dual interaction. This configuration corresponds to notch filters which has enabled the development of many applications, including optical logic processing [14], spectral imaging [15], double-pass filtering [16], and wide-angle modulation [17]. This particular configuration corresponds to the situation when the exact synchronism conditions are satisfied simultaneously for the ordinary and the extraordinary beams. In the case of incident polarization collinear to the interaction plane, the incident optical wave vector $\mathbf{k_i}$ is coupled to the extraordinary mode. The diffracted optical wave vector $\mathbf{k_{d-}}$ is then coupled to the ordinary mode. Conversely, in the case of incident polarization orthogonal to the interaction plane, the incident optical wave vector $\mathbf{k_i}$ is coupled to the ordinary mode. The diffracted optical wave vector $\mathbf{k_{d+}}$ is then coupled to the extraordinary mode. The incident and diffracted optical beams are angularly separated with $\theta_{d-} < \theta_l < \theta_{d+}$. The dual interaction condition is obtained for a given acoustic frequency and for a certain angle of incidence θ_i. The wave vector diagram of the dual interaction is close to the classical noncritical phase matching (NPM) interaction. Frequency and spectral bandwidths of the same order of magnitude are thus obtained. The frequency bandwidth is proportional to the inverse of the interaction effective length, W_{eff}. This can be deduced from the expression of the diffraction efficiency of the acousto-optic interaction, η [13]:

$$\eta = \frac{P}{P_0} \frac{\sin^2\left(\frac{\pi}{2}\sqrt{\frac{P}{P_0} + \left(\frac{\Delta\Phi}{\pi}\right)^2}\right)}{\frac{P}{P_0} + \left(\frac{\Delta\Phi}{\pi}\right)^2},$$

with P being the power of the acoustic wave, P_0 being the power required to obtain maximum efficiency, and $\Delta\Phi$ being

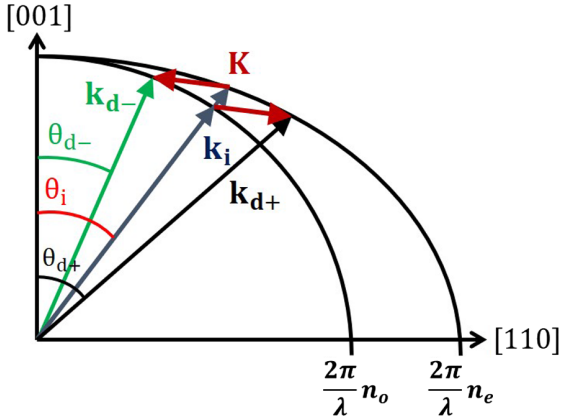

Fig. 2. Wave vector diagram for the simultaneous diffraction in the case of dual interaction.

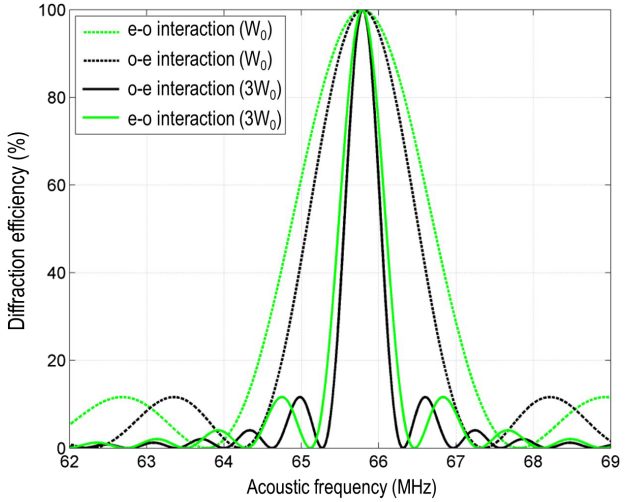

Fig. 3. Comparison of the RF bandwidth evolution when tripling the interaction length.

the phase mismatch parameter of the interaction which is the expression of an offset from synchronism conditions: $\Delta\Phi = \Delta k_d \cdot W_{\text{eff}}$, resulting from an offset from the momentum matching condition, Δk_d.

3. CASE OF DUAL DIFFRACTION WITH MULTI-ELECTRODE DEVICE

Considering that the interaction length is related to the transducer length, a transducer of length $3W_O$ will produce a frequency bandwidth three times lower than a transducer of length W_O. The same type of relationship is valid for the optical bandwidth. (This first-order approximation is no longer valid for short wavelengths in the near UV.) We compare in Fig. 3 the interaction RF bandwidth with length W_O corresponding to the case of one electrode and with the interaction length $3W_O$ corresponding to the case of three electrodes; this corresponds, for example, to a configuration with three identical electrodes.

Taking into consideration the asynchrony conditions which differ depending on whether we study the extraordinary-to-ordinary (e-o) or the ordinary-to-extraordinary (o-e) interaction, the frequency bandwidths of the two interactions are different [18]. We always obtain $\Delta f_{0-e} < \Delta f_{e-0}$. Figure 3 represents the frequency bandwidths Δf_{0-e} and Δf_{e-0} during the dual interaction for the wavelength $\lambda_O = 593$ nm and the acoustic cut $\theta_a = 6°$. In this configuration, we obtain $\Delta f_{0-e} \approx 0.7\,\Delta f_{e-0}$.

The interest of a multi-electrode component is therefore obvious: it enables us to adjust the bandwidth, thanks to the interaction length, according to the wavelength we wish to filter. When it is necessary, the electrodes are activated simultaneously to increase the interaction length and reduce the filtering bandwidth. In this case, it is necessary to ensure that the acoustic waves propagating in the crystal are in phase.

Figure 3 also shows that, when we triple the interaction length, the RF frequency bandwidth is reduced, but sidelobes are present. This is because a homogeneous diffraction grating is considered, corresponding to the case when the same RF power is applied to each electrode of the device with three electrodes. However, it is possible to reduce (or increase) the intensity of the diffracted sidelobes by modulating the RF power applied to each electrode, resulting in the apodization of the sound field [19]. Hence, the second advantage of the multi-electrode configuration is that the overall acoustic response of the transducer can be modified by adjusting the distribution of acoustic power by adjusting the RF levels over the different electrodes.

The determination of the synchronism conditions of the dual interaction is done by determining the point of intersection of the synchronism curves of the extraordinary-to-ordinary interaction (e-o) and the ordinary-to-ordinary interaction (o-e). In Fig. 4, we depict the acoustic frequency evolution as a function of the incident optical angle (at synchronism conditions) for the acoustic cut $\theta_a = 6°$ and for two outer wavelengths of the visible band: 400 and 650 nm. The green curves correspond to the extraordinary to ordinary (e-o) interaction, and the black curves correspond to the ordinary to extraordinary (o-e) interaction. As the intersection of the (e-o) and (o-e) curves, the operating zone of the dual interaction is located between the two horizontal asymptotes of the curves (which correspond to the conditions of the NPM interaction).

The evolution of the synchronism frequencies and the incident and diffracted optical angles as a function of the wavelength is a typical case of the NPM interaction. As the wavelength increases, the synchronism frequency decreases. In the example of Fig. 4, we obtain for $\lambda_O = 400$ nm, $\theta_i = 13.2°$, $f_O = 129.3$ MHz and for $\lambda_O = 650$ nm, $\theta_i = 13.05°$, $f_O = 65.8$ MHz. For these two wavelengths, the incident angle determining the double interaction differs slightly. In practice, this means that a filter cannot be perfectly oriented for the entire spectral band of interest. During the design process, it is possible to select an average incident angle θ_i.

The theoretical values of the frequency responses (e-o) and (o-e) are presented in Fig. 5 and in Fig. 6 for an average incident optical angle $\theta_i = 13.1°$. Figure 5 corresponds to the frequency response of the filter for $\lambda_O = 400$ nm, while Fig. 6 corresponds to the frequency response of the filter for $\lambda_O = 650$ nm. With the average incident angle chosen, which does not correspond to the optimal one for any of the two wavelengths, we consequently observe a shift in the synchronous frequency, depending on

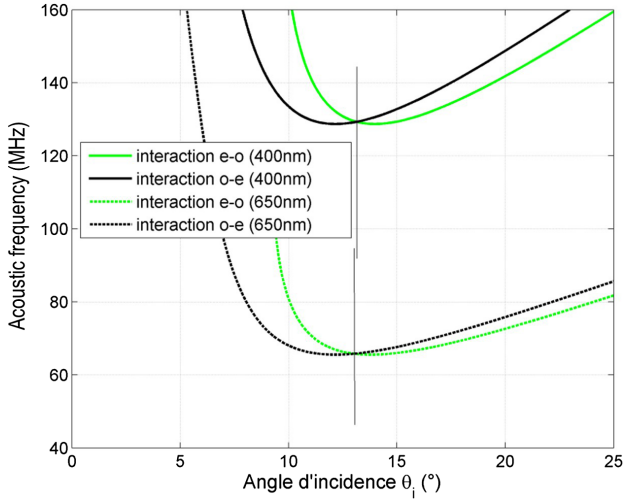

Fig. 4. Evolution of the acoustic frequency as a function of the incident angle at synchronism.

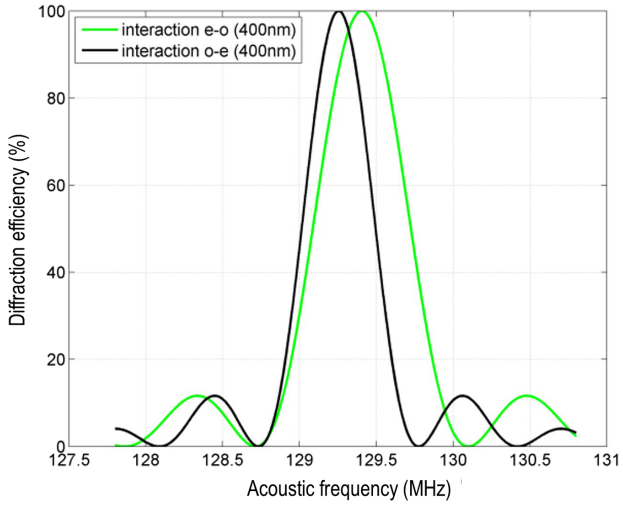

Fig. 5. Diffraction efficiency around the synchronism frequency for a 400 nm wavelength.

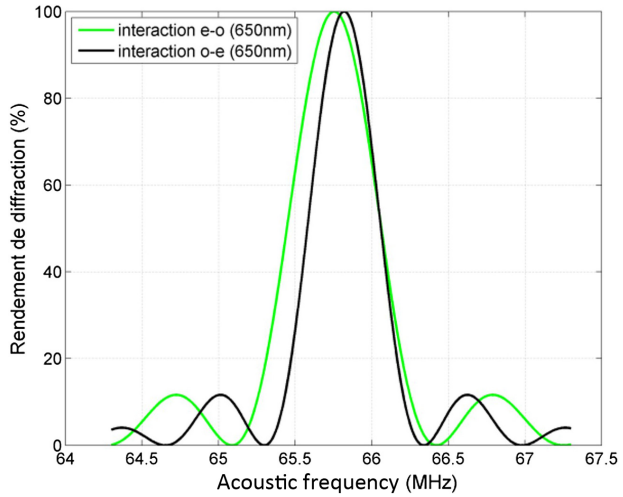

Fig. 6. Diffraction efficiency around the synchronism frequency for a 650 nm wavelength.

whether the incident optical beam is coupled to the ordinary (black o-e curve) or extraordinary mode (green e-o curve). For $\lambda_O = 400$ nm, the synchronism frequency of the ordinary-to-extraordinary interaction (o-e) is lower than the synchronism frequency of the extraordinary-to-ordinary interaction (e-o), while the opposite occurs for $\lambda_O = 650$ nm. Nevertheless, small shifts are observed (0.15 MHz for $\lambda_O = 400$ nm and 0.07 MHz for $\lambda_O = 650$ nm), which still allows interesting diffraction efficiencies to be obtained at the determined synchronism frequencies of Fig. 4 ($f_0 = 65.8$ MHz and $f_0 = 129.3$ MHz). We also observe that the frequency (and therefore optical) bandwidths are not affected by this effect. However, RF frequency tuning associated to the choice of an optimized incident angle enables us to extend the filtering capability [20].

4. DESIGN OF A TRIPLE-ELECTRODE ACOUSTO-OPTICAL TUNABLE FILTER

The interaction length W_{eff} is directly related as explained to the transducer length, which corresponds more precisely to the electrode length. A large number of electrodes of all different dimensions would induce many possibilities of variations in the optical bandwidth $\Delta\lambda$. However, in this feasibility study, the aim is to obtain a system that can be produced with standard industrial process and can be driven with simple RF generators. For this purpose, we have chosen a three-electrode configuration of identical dimensions. In the following, we restrict ourselves to three electrodes and evaluate the possibility to obtain the satisfactory results in terms of apodization and homogenization of the optical bandwidth.

Figure 7 shows the simulated optical bandwidths for three different interaction lengths: 3, 6, and 9 mm. There are three 3 mm electrodes that can be independently activated. The blue curves correspond to the activation of only one electrode, the red curves correspond to the activation of two electrodes, and the green curves correspond to the activation of all three electrodes simultaneously. In the same way that the frequency bandwidth of the (e-o) and (o-e) interactions differ, the optical bandwidths $\Delta\lambda_{o\text{-}e}$ (solid line) and $\Delta\lambda_{e\text{-}o}$ (dashed line) are related by $\Delta\lambda_{o\text{-}e} \approx 0.7 * \Delta\lambda_{e\text{-}o}$.

As an example, for the interaction (o-e) and for $W = 3$ mm, the optical bandwidth of the component varies from 2.6 to 12 nm between 400 and 650 nm, which corresponds to an increase of a factor of 4.6. Theoretically, five electrodes of the same size would be required to achieve the same optical bandwidth along the spectral range of interest. We can deduct from Fig. 6 that, with the activation of one, then two and finally three electrodes, we can obtain an optical bandwidth with a "sawtooth" profile. For shorter wavelengths, between 400 and 488 nm, with one electrode activated, the bandwidth is between 3.9 and 7.7 nm (for the extraordinary-to-ordinary interaction, dashed lines). With two electrodes activated, we obtain between 488 and 593 nm; finally, with three electrodes, we obtain between 593 and 671 nm. By the same procedure, the optical bandwidth $\Delta\lambda_{o\text{-}e}$ varies between 2.6 and 5.3 nm for the

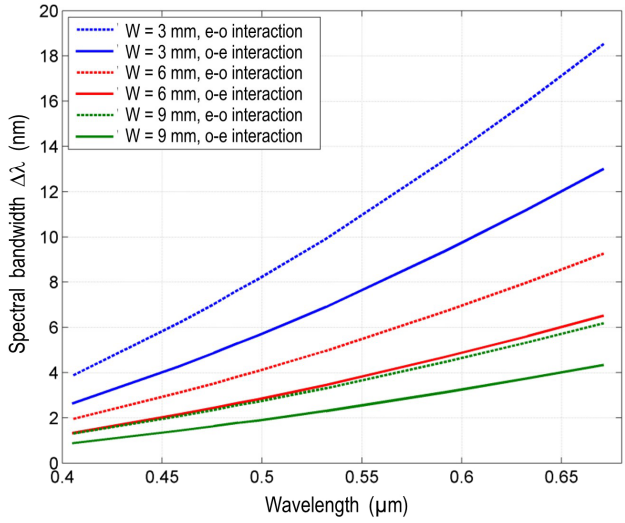

Fig. 7. Optical bandwidth evolution as a function of the wavelength.

ordinary to extraordinary interaction (solid lines). The increase in the optical bandwidth is thus limited to a factor of 2 in both cases. Note that, for the results presented here, we consider the activation of one or more electrodes by applying the same RF power in each channel, i.e., without seeking apodization.

5. EXPERIMENTAL VALIDATION AND DISCUSSION

The prototype technical characteristics are summarized in Table 1. The experimental characterization was carried out using the optical line of the experimental bench presented in Fig. 8: six laser sources deliver 10 distinct optical wavelengths: from 405 to 671 nm. The dual interaction filter is oriented so that the beams from the lasers are at normal incidence to the optical input face of the component. The prototype is mounted on micrometric mounts in order to finely adjust the angle of incidence θ_i when searching for the double interaction. The radiofrequency (RF) part requires three symmetrical channels in order to keep the transducers operating in phase. A power divider distributes the RF power at the output of the synthesizer to the three transducer channels (−6 dB loss). Three identical amplifiers (AA AMPA-B-30) increase the level by 34 dB. Finally, three identical attenuators adjust the power applied to each channel of the acousto-optic filter (each electrode) from 0 to −20 dB in 1 dB steps, and a phase control on the central electrode is also introduced as a mean to prevent overmodulation [21]. The power levels of the three channels are compared using a spectrum analyzer. In order to determine the interaction efficiency (e-o) and (o-e), polarization rotation blades (45° or 90°) are positioned upstream of the acousto-optic filter. Thanks to this setup the filtering characteristics and apodization ability have been validated experimentally, as depicted by Figs. 9 and 10. They present the evolution of the diffraction efficiency as a function of the acoustic frequency. For these figures, the ordinary mode was coupled with a laser of the wavelength

Table 1. Characteristics of the Dual-Interaction Multi-electrode Acousto-Optic Filter

Optical range (nm)	[400, 650]
Optical incident angle (°)	13.1
Acoustic cut angle θ_a (°)	6
Acoustic velocity V_{ac} (m/s)	658
Acoustic obliquity Ψ_a (°)	44.3
Acoustic frequency (MHz)	[65, 130]
Electrode width [W_1, W_2, W_3] (mm)	[3, 3, 3]
ΔF: extraordinary to ordinary (MHz)	2.09 at $W = 3$ mm
	1.05 at $W = 6$ mm
	0.71 at $W = 9$ mm
ΔF: ordinary to extraordinary (MHz)	1.58 at $W = 3$ mm
	0.8 at $W = 6$ mm
	0.54 at $W = 9$ mm
Δλ: extraordinary to ordinary (nm)	1.2–3.6 at 400 nm
	5.7–17.1 at 650 nm
Δλ: ordinary to extraordinary (nm)	0.8–2.5 at 400 nm
	4–12 at 650 nm
$\Delta\theta$: Angular aperture, −3 dB, out of crystal (°)	≈2.5 at 400 nm
	≈4 at 650 nm
Filter rejection ratio (dB)	≤20

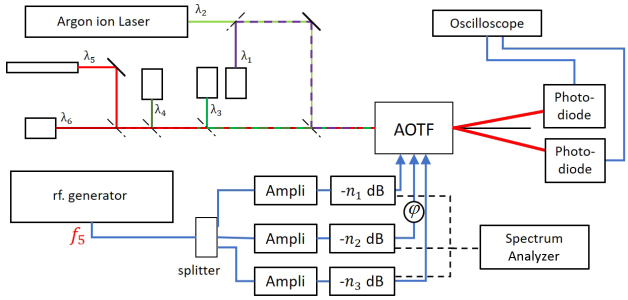

Fig. 8. Experimental setup.

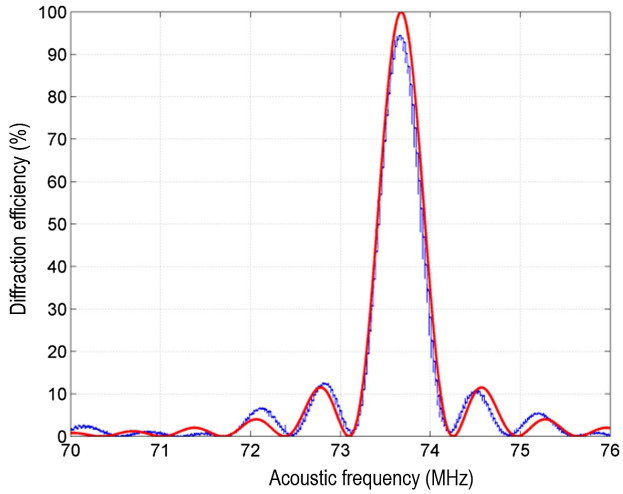

Fig. 9. Diffraction efficiency; red plot: theoretical characteristics, blue plot: experimental characteristics for a wavelength of 593 nm.

$\lambda_0 = 593$ nm. Figure 9 depicts the reference case for which no apodization is sought: the same power is applied on the three electrodes; as can be seen, the sidelobes are significant and peak at a relative height of 13%. Secondary sidelobes can also be seen, their relative amplitude peak at 6%, can also be seen. Figure 10 corresponds to the case when the relative power on the side electrodes is reduced by 4 dB compared to the power of the central electrode. It corresponds to the situation with the adjacent sidelobes reduced to a very low value: 2%, together with the secondary sidelobes almost not pushed up. The experimental values are collected in Table 2. They are obtained in different experimental situations, starting from the reference case with no apodization and then reducing relatively the power on the side electrodes down to −8 dB. During the experimental procedure, the power on the central electrode was adjusted to maintain a diffraction efficiency close do 90%. As can be seen on Fig. 11, it is possible to cancel out the first sidelobe (relative power on the side electrodes is reduced by 6 dB). As can be seen from Table 2, the adjacent sidelobes can be drastically attenuated. As for the secondary sidelobes, they are measured to be close to 6%; then their amplitude rises to 7%–8%.

The attenuators allow the fine control of each one of the three channels independently. This requires the knowledge of the characteristics of the various elements: each transducer has its own custom electrical impedance network, which is optimized to work in a specific frequency range, mostly limited to one octave. Although comparable, these three impedance networks

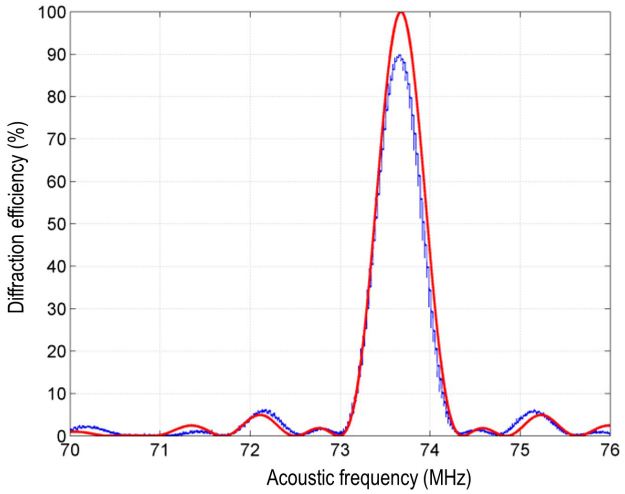

Fig. 10. Diffraction efficiency with apodization (−4 dB drive); red plot: theoretical characteristics, blue plot: experimental characteristics for a wavelength of 593 nm.

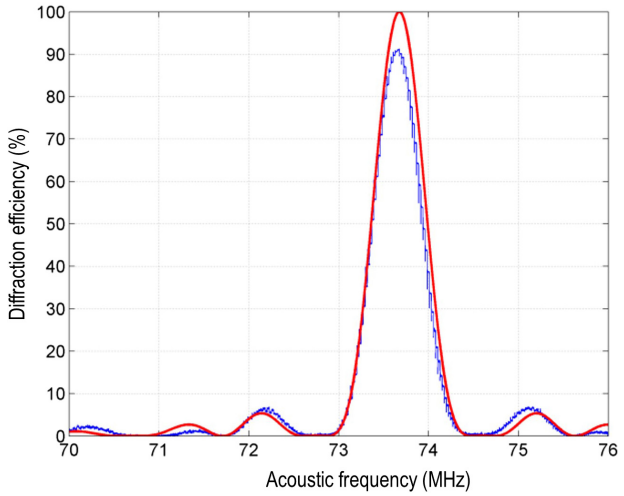

Fig. 11. Diffraction efficiency with apodization (−6 dB drive); red plot: theoretical characteristics, blue plot: experimental characteristics for a wavelength of 593 nm.

Table 2. Experimental Characteristics of Apodization at $\lambda_0 = 593$ nm

Side Electrode Delta Power (dB)	Central RF Power at 90% Efficiency (dBm)	Sidelobe Intensity (%)	Second Sidelobe Intensity (%)
0	13.5	13	6
−1	13.8	8	6
−2	14.3	6	6
−3	14.5	4	6
−4	15.2	2	7
−6	16	∼0	8
−8	16.9	∼0	8

are not identical. Because these networks make use of lumped components, a part of the applied RF energy is reflected back towards the RF setup, creating an RF amplitude inhomogeneity. Consequently, a characterization of the three transducers from an electrical point-of-view is necessary. The obtained results will give a more detailed view on how much RF energy is physically applied to the transducer itself and consequently transformed into sound waves. Hence, the applied RF signal should be made adaptable using the variable attenuator setup depicted in Fig. 8.

As part of future work, this RF driving setup should be optimized and automatized in order to drive the multi-transducer setup in a more accurate and fast way. For accurate and swift RF frequency switching, several generator principles exist: a phase-locked loop-based design [22], a direct digital synthesis approach [23], or a Hilbert transform-based generator [24]. Additionally, an automated flexible RF amplifier setup, integrated or separate from the RF generator, is mandatory for achieving a more optimal optical efficiency. By making the power level of this RF amplifier adaptable, a compensation can be done for the reflected power due to the RF amplitude inhomogeneity. In common RF driving setups, this compensation is not implemented. Having a combination of characterized transducers, flexible RF generators and adaptable RF amplifiers will create the possibility to design a resilient RF driving system optimized for compensating power reflections and hence create a higher optical efficiency.

6. CONCLUSION

In this paper, we have reported the design and experimental validation of a three-electrode acousto-optic filter that is able to operate with arbitrary polarized light. Multi-electrode technology offers an additional degree of freedom by allowing the optical bandwidth of an acousto-optical component to be modulated. Moreover, the filtering characteristics can be improved, thanks to the apodization process. Detailed experimental results showing that a significant reduction of sidelobes is possible are presented. Such a system would benefit from a multi-channel tunable RF generator with individual control of the amplitude and phase. It will now be useful for an analysis of partially polarized light with a continuous spectrum.

Disclosures. The authors declare no conflicts of interest.

Data availability. Data underlying the results presented in this paper are not publicly available at this time but may be obtained from the authors upon reasonable request.

REFERENCES

1. J. Melngailis, A. A. Maradudin, and A. Seeger, "Diffraction of light by ultrasound in anharmonic crystals," Phys. Rev. **131**, 1972–1975 (1963).
2. A. Korpel, "Acousto-optics," Appl. Solid State Sci. **3**, 71–180 (1972).
3. N. Savage, "Acousto-optic devices," Nat. Photonics **4**, 728–729 (2010).
4. S. E. Harris and R. W. Wallace, "Acousto-optic tunable filter," J. Opt. Soc. Am. **59**, 744–747 (1969).
5. I. C. Chang, "Noncollinear acousto-optic filter with large angular aperture," Appl. Phys. Lett. **25**, 370–372 (1974).
6. T. Yano and A. Watanabe, "Acoustooptic TeO_2 tunable filter using far-off-axis anisotropic Bragg diffraction," Appl. Opt. **15**, 2250–2258 (1976).
7. I. C. Chang, "Acousto-optic tunable filters," Opt. Eng. **20**, 824–829 (1981).
8. K. B. Yushkov and N. F. Naumenko, "Optical beam diffraction tensor in birefringent crystals," J. Opt. **23**, 095602 (2021).

9. D. Zawada, G. Franssens, R. Loughman, *et al.*, "Systematic comparison of vectorial spherical radiative transfer models in limb scattering geometry," Atmos. Meas. Tech. **14**, 3953–3972 (2021).
10. E. Dekemper, N. Loodts, B. Van Opstal, *et al.*, "Tunable acousto-optic spectral imager for atmospheric composition measurements in the visible spectral domain," Appl. Opt. **51**, 6259–6267 (2012).
11. V. B. Voloshinov and V. Y. Molchanov, "Acousto-optical modulation of radiation with arbitrary polarization direction," Opt. Laser Technol. **27**, 307–313 (1995).
12. Z. Yuanfeng and Y. Jisheng, "Optimization and design of acousto-optic tunable filters," J. Optoelectron. Adv. Mater. **7**, 1599–1604 (2005).
13. I. C. Chang, "Acousto-optic devices and applications," in *Handbook of Optics* (1995), Vol. **2**, pp. 1–54.
14. H. Lee, "Polarization-independent acoustooptic light modulation with large angular aperture," Appl. Opt. **27**, 815–817 (1988).
15. N. Gupta and D. R. Suhre, "Notch filtering using a multiple passband AOTF in the SWIR region," Appl. Opt. **55**, 7855–7860 (2016).
16. J. Champagne, J. C. Kastelik, S. Dupont, *et al.*, "Study of the spectral bandwidth of a double-pass acousto-optic system," Appl. Opt. **57**, C49–C55 (2018).
17. S. N. Antonov, "Wide-angle polarization-independent paratellurite-based acousto-optic laser radiation modulator," Acoust. Phys. **66**, 5–11 (2020).
18. D. Glenar, J. J. Hillman, B. Saif, *et al.*, "Acousto-optic imaging spectropolarimetry for remote sensing," Appl. Opt. **33**, 7412–7424 (1994).
19. R. Pieper, A. Korpel, and W. Hereman, "Extension of the acousto-optic Bragg regime through Hamming apodization of the sound field," J. Opt. Soc. Am. A **3**, 1608–1619 (1986).
20. S. Dupont, J. Champagne, and J. C. Kastelik, "Equal-efficiency diffraction of unpolarized wideband light with acousto-optic filters," J. Mod. Opt. **69**, 718–727 (2022).
21. S. N. Antonov, A. V. Vainer, V. V. Proklov, *et al.*, "Acoustooptic Bragg diffraction without overemodulation with a phased-array transducer," Tech. Phys. **55**, 1336–1342 (2010).
22. J. Vanhamel and D. Stutman, "The design of a flexible RF generator for driving acousto-optical devices in space applications," J. Phys. Conf. Ser. **2526**, 012120 (2022).
23. J. Tierney, C. Rader, and B. Gold, "A digital frequency synthesizer," IEEE Trans. Audio Electroacoust. **19**, 48–57 (1971).
24. J. Vanhamel, D. Fussen, E. Dekemper, *et al.*, "RF-driving of acoustic-optical tunable filters; design, realization and qualification of analog and digital modules for ESA," Microelectron. Reliab. **55**, 2103–2107 (2015).